Pilot Detection and Location of Broken Conductor Faults for Tapped Transmission Lines

Milad Beikbabaei, Austin Dempsey, Brady Alexander, and Ali Mehrizi-Sani

***Abstract*—The increasing integration of inverter-based resources (IBR) introduces the need for new protection methods to detect open-circuit faults, such as broken conductor faults. Fast and reliable detection of broken conductor faults is critical, since an undetected fault can lead to wildfire. The presence of tapped lines in a transmission grid introduces further protection challenges since the measured current does not drop significantly compared to a scenario without tapped lines. Moreover, tapped transmission line measurements are not always available, making protection even more challenging. If a fault is located on a tapped line, only the tapped line needs to be disconnected, so locating the fault helps disconnect only the minimal affected area and increase the reliability of the grid. Most previous work does not study broken conductor faults with the presence of IBRs and tapped lines and does not propose ways to locate the fault. This work proposes a communication-based protection algorithm that can detect the broken conductor in a transmission system with tapped lines. The algorithm detects the fault in less than 55 ms and locates the fault accurately. The proposed method is tested under various cases in the modified IEEE 9-bus system with two grid-following IBRs using PSCAD/EMTDC.**

***Keywords*—Broken conductor, inverter-based resources (IBR), inverter, power system protection, single-phase line break fault.**

I. Introduction

The power grid is transitioning toward the use of more renewable inverter-based resources (IBR). This integration of IBRs introduces new challenges for the protection of the grid against different faults, such as short-circuit and open-circuit faults, mainly due to the low fault current limit of IBRs, up to 20% of the nominal current, and the lack of negative sequence current from IBRs [1], [2]. As a result, new protection schemes need to be developed to detect faults in a grid with high penetration of IBRs [3]. Most work focuses on detecting and locating short-circuit faults; however, open-circuit faults can also occur in the power system [4].

Open-circuit faults can occur as a result of a breaker malfunction or a broken conductor [5], [6], and an undetected broken conductor can initiate wildfires. High impedance faults (HIF) occur when a tree branch contacts a power line, creating a current path to the ground through the vegetation. If a HIF remains undetected, it can lead to a highly destructive wildfire [7], [8]. Moreover, HIF detection is a challenging task, mainly due to the randomness in current magnitude, arc intermittence, and nonlinearity [9]–[11]. Wildfires are occurring more often, primarily due to global warming; in 2050, wildfires are predicted to happen twice as often compared to 2015 [12], [13]. In 2021 alone, 58,985 wildfire occurred, affecting almost 4,096 hectares [14]. As a result, it is essential to develop fast open circuit detection techniques that work with IBR-dominated grids.

Reference [15] reports a broken conductor event in one of the phases of a 220 kV transmission system, located 8 km from the substation. Broken conductor faults need to be detected and located. Most broken conductor detection techniques focus on distribution grids and not transmission systems; however, transmission systems are susceptible to broken conductors as well [16]–[18]. A tapped line is connected in parallel to a line, often as a temporary connection where the measurements are unavailable. Having a tapped transmission line makes open-circuit fault detection more challenging. If the faults occurs in the tapped line, the relay current of the affected phase does not drop significantly since it still goes to the other bus. Moreover, the electrical measurements of the tapped line are not always available.

Conventional broken conductor techniques rely on the ratio of the negative to positive sequence current, which can take up to tens of seconds [15]. Reference [1] develops a broken conductor detection method that relies only on local measurements; however, the proposed method takes at least 300 ms to detect the fault. In [19], a pilot protection algorithm is developed for a hybrid HVDC transmission line. Reference [15] develops a broken conductor detection method that can detect a broken conductor 400 ms after the fault occurrence.

Communication is widely used in power grids and can help with the development of fast and reliable protection techniques. For example, communication is used in line differential protection [20]–[22]. Reference [23] develops a communication-based protection scheme for grids with high penetration of photovoltaic resources. Furthermore, utilities are connecting optical fiber cables to utility devices and solar and wind systems for remote control, monitoring, and protection of the grid, which can increase grid resiliency [24]. Exchanging data between the two buses on either side of a tapped line facilitates fast and reliable broken conductor fault protection. This work proposes a pilot broken conductor

This work is supported in part by the National Science Foundation (NSF) under award ECCS-1953213, in part by the U.S. Department of Energy's Office of Energy Efficiency and Renewable Energy (EERE) under the Solar Energy Technologies Office Award Number 38637 (UNIFI Consortium led by NREL), and in part by Manitoba Hydro International. The views expressed herein do not necessarily represent the views of the U.S. Department of Energy or the United States Government.

M. Beikbabaei, A. Dempsey, B. Alexander, and A. Mehrizi-Sani are with the Bradley Department of Electrical and Computer Engineering, Virginia Polytechnic Institute and State University, Blacksburg VA 24061 USA. (e-mails: miladb@vt.edu, ajd02@vt.edu, bradyba19@vt.edu, mehrizi@vt.edu).

Paper submitted to the International Conference on Power Systems Transients (IPST2025) in Guadalajara, Mexico, June 08-12, 2025.

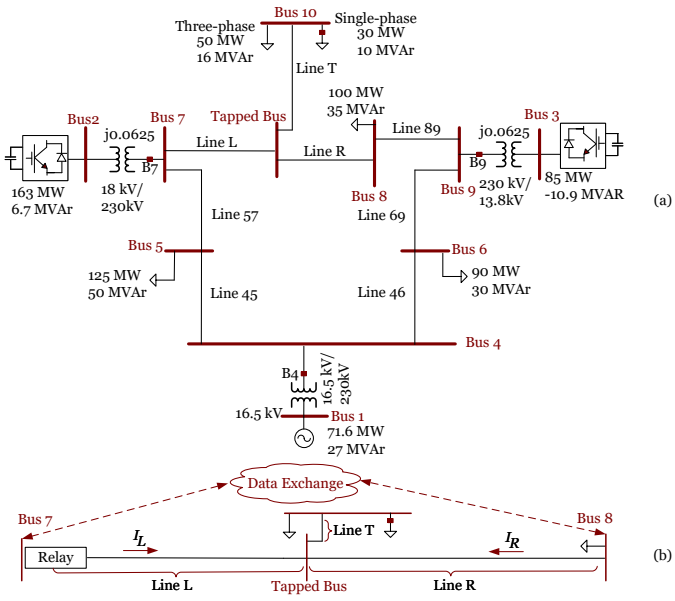

Fig. 1. Single line diagram of: (a) IEEE 9-bus system and (b) the relay placement and data exchange path.

protection method that successfully detects and locates the fault, with the following salient features:

- The proposed method successfully detects the fault at tapped lines.
- The broken conductor fault is detected within 55 ms of the fault occurrence.
- The proposed method works with transmission systems with high penetration of IBRs.

The rest of the paper is structured as follows. Section II is the test system, Section III is the methodology, Section IV discusses the performance evaluation, and Section V concludes the paper.

II. Test System

The IEEE 9-bus system is modified by adding two IBRs and a tapped line between buses 7 and 8 in PSCAD/EMTDC, as shown in Fig. 1(a) [25]. A three-phase 50 MW and 16 MVAR load and a dispatchable single-phase 30 MW and 10 MVAR load are connected to Bus 10. Broken conductor and short-circuit faults are applied at Lines L, R, and T, as shown in Table I. The changes in the RMS values of the three-phase currents of Lines L and R, the measured impedance angles for phase a of buses 7 and 8, and the ratios of the bus 7 and 8 current magnitudes per phase are recorded. Analyzing the changes in Table I helps with developing broken conductor detection for each line segment.

IBRs are connected to the grid through a 0.1 Ω resistance and a 1.885 Ω inductance. The IBR's nominal terminal output voltage is 18 kV, converted to 230 kV using a step-up transformer, where the primary group winding is Δ and the secondary side is a star with a grounded neutral. The proportional gain of the power controller is 0.5, and the integrator time constant is 0.01. The proportional gain of the current controller loop is 1.5, and the integrator time constant

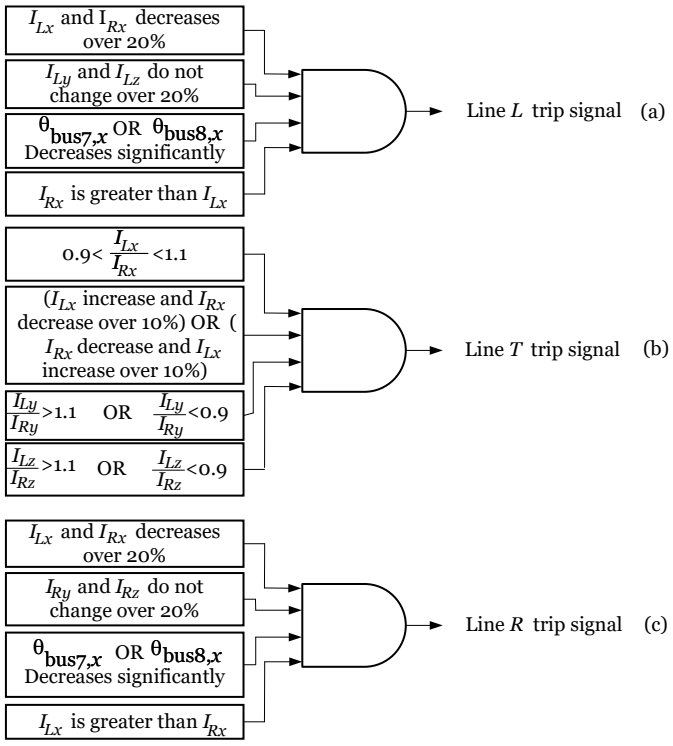

Fig. 2. Logic for relay placed at Bus 7 to locate phase x broken conductor fault at: (a) Line L, (b) Line T, and (c) Line R.

is 0.05. The PLL proportional gain is 50, and the PLL integral gain is 900. The nominal powers of the IBRs connected to buses 2 and 3 are 192 MVA and 128 MVA, respectively. IBRs connected to buses 2 and 3 inject 163 MW and 6.7 MVAR and 85 MW and -10.9 MVAR, respectively.

III. Methodology

The proposed method can detect and locate the broken conductor fault for a tapped line, where the fault can be located before, after, or on the tapped line. Furthermore, each line has its own fault detection logic, allowing the fault to be located. The method utilizes communication, where each bus sends the current magnitude and angle to the other buses, and the measurement is required to be synchronized as shown in Fig. 1(b). Table I indicates that in the event of a broken conductor in phase a of Line L, the current magnitude decreases, I_{Ra} becomes greater than I_{La} since it can circulate through the tapped line, and the measured impedance angle of phase a decreases since only the line capacitive charge is left in the phase. Fig. 2 shows the generic format of the proposed logic located at Bus 7 for detecting the broken conductor fault for phase x before, within, and after the tapped line. For instance, for detecting broken conductor faults for phase b, x is replaced with b, and y and z are replaced with a and c. The logic shown in Fig. 2(a) detects a broken conductor at Line L if both I_{Lx} and I_{Rx} decrease, I_{Ly} and I_{Lz} do not change over 20%, $\theta_{bus7,x}$ or $\theta_{bus8,x}$ decreases significantly, and I_{Rx} becomes greater than I_{Lx}.

Table I indicates that during a broken conductor fault in phase a of Line T, the magnitudes of I_{Ra} and I_{La} become

TABLE I
MEASUREMENT CHANGES UNDER VARIOUS BROKEN CONDUCTOR AND SHORT-CIRCUIT FAULTS

Fault	Location	I_{La}	I_{Lb}	I_{Lc}	I_{Ra}	I_{Rb}	I_{Rc}	θ_{Bus7}	θ_{Bus8}	$\frac{I_{La}}{I_{Ra}}$	$\frac{I_{Lb}}{I_{Rb}}$	$\frac{I_{Lc}}{I_{Rc}}$
Broken conductor	Line L phase A	↓	-	-	↓	-	-	↓	↓	↓	-	-
	Line T phase A	↓	-	-	↑	-	-	-	-	↓	↓	↓
	Line R phase A	↓	-	-	↓	-	-	↓	↓	↑	-	-
Short circuit	Line L AG	↓	-	-	↓	-	-	↓	-	↑	-	-
	Line L BG	-	↓	-	-	↓	-	↑	↓	-	↑	-
	Line L ABG	↑	↓	↓	↑	↓	↓	↑	↓	↑	-	-
	Line L BCG	-	↓	↓	-	↓	↓	↓	↑	-	↑	-
	Line L $ABCG$	↓	↓	↓	↓	↓	↓	↓	↑	-	-	-
Short circuit	Line T AG	↑	-	-	↓	-	-	↑	↑	↑	-	-
	Line T BG	-	↑	-	-	↓	-	↓	↑	-	↑	-
	Line T ABG	↑	↑	-	↓	↓	-	↓	↓	↑	↑	-
	Line T BCG	-	↑	↑	-	↓	↓	↓	↑	-	↑	-
	Line T $ABCG$	↑	↑	↑	↓	↓	↓	-	↑	-	-	-
Short circuit	Line R AG	↑	-	-	↑	-	-	↑	↑	↓	-	-
	Line R BG	-	↑	-	-	↑	-	↓	↑	-	↓	-
	Line R ABG	↑	↑	-	↑	↑	-	↓	↑	↓	↓	-
	Line R BCG	-	↑	↑	-	↑	↑	↓	↑	-	↓	↓
	Line R $ABCG$	↑	↑	↑	↑	↑	↑	-	-	↓	↓	↓

close since the only difference between them is a result of the line capacitive current charge. Moreover, the current magnitude decreases for one of the buses and increases for the other. In addition, the other current ratios of phases b and c do not change significantly and are lower than 0.9 or greater than 1.1. The logic shown in Fig. 2(b) detects a broken conductor at phase x of Line L if $0.9 < \frac{I_{Lx}}{I_{Rx}} < 1.1$, I_{Lx} increases while I_{Rx} decreases or I_{Lx} decreases while I_{Rx} increases, $0.9 > \frac{I_{Ly}}{I_{Ry}}$ or $\frac{I_{Ly}}{I_{Ry}} > 1.1$, and $0.9 > \frac{I_{Lz}}{I_{Rz}}$ or $\frac{I_{Lz}}{I_{Rz}} > 1.1$.

Table I indicates that in a broken conductor fault in phase a of Line R, the current magnitude decreases, I_{La} becomes greater than I_{Ra} since it can circulate current through the tapped line, and the measured impedance angle decreases since only the line capacitive charge is left. Fig. 2(c) detects a broken conductor at phase x of Line R if both I_{Lx} and I_{Rx} decrease, I_{Ry} and I_{Rz} do not change over 20%, $\theta_{bus7,x}$ or $\theta_{bus8,x}$ decreases significantly, and I_{Lx} becomes greater than I_{Rx}.

IV. PERFORMANCE EVALUATION

The effectiveness of the proposed method is tested for broken conductor faults at Lines L, R, and T. Furthermore, the effectiveness of the proposed method is investigated for single-phase load disconnection, broken conductor fault at adjacent lines, and short-circuit faults to ensure the security of the proposed protection logic.

A. Broken Conductor at Line L

Fig. 3 shows results for a broken conductor fault at Line L occurring at $t = 10$ ms. Fig. 3(a) shows the three-phase current of Line L, where the phase a current decreases significantly after the broken conductor fault occurs; however, the other two phases do not change significantly. Fig. 3(b) shows the three-phase current at Line R, where the phase a current

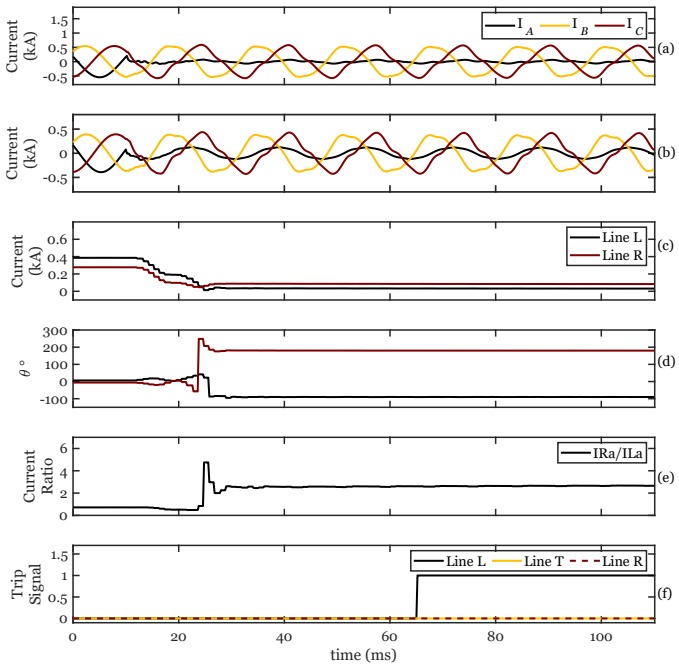

Fig. 3. Simulation results for broken conductor at Line L: (a) Line L instantaneous current, (b) Line R instantaneous current, (c) Lines L and R phase a RMS current, (d) impedance angle for phase a, (e) $\frac{I_{Ra}}{I_{La}}$, and (f) the trip signals.

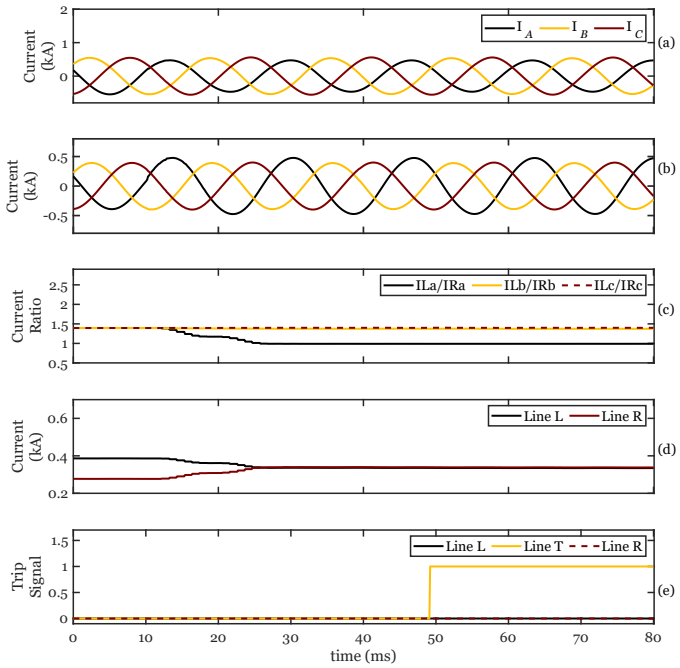

Fig. 4. Simulation results for broken conductor at Line T: (a) Line L instantaneous current, (b) Line R instantaneous current, (c) $\frac{I_L}{I_R}$, (d) Lines L and R phase a RMS current, and (e) the trip signals.

decreases to 27.95% of its pre-fault value since the current can go to the tapped line; however, the other two phases do not change significantly. Fig. 3(c) shows the RMS values of the phase a current of buses 7 and 8, where I_{La} decreases from 0.386 kA to 0.031 kA and I_{Ra} decreases from 0.277 kA to 0.086 kA and Fig. 3(d) shows the phase a impedance angle seen from buses 7 and 8, where θ_{Bus7a} decreases from 6.36° to $-89°$ and θ_{Bus8a} increases from $-6.13°$ to 179.96°. Fig. 3(e) shows the ratio of the phase a current magnitude of bus 8 to that of bus 7. Fig. 3(f) shows the trip signal for each algorithm, where only Line L detects a broken conductor 55 ms after the fault occurrence. The Line T and R algorithms correctly do not detect a broken conductor fault.

B. Broken Conductor at Tapped Line

Fig. 4 shows results for a broken conductor fault at phase a of Line T, the tapped line, occurring at $t = 10$ ms. Fig. 4(a) and (b) show the three-phase current of Lines L and R, respectively, where only the phase a current changes significantly. Fig. 4(c) shows the ratio of Line L per phase current to Line R per phase current, where the phase a current ratio decreases from 1.39 to 0.989; however, the other two phases do not change significantly. The ratio falls between 0.9 and 1.1, which is one of the conditions for detecting a broken conductor in the tapped line. Fig. 4(d) shows that the RMS values of the phase a currents of Lines L and R become close after the broken conductor occurs, reaching 0.335 and 0.339 kA. Fig. 4(e) shows the trip signal for each algorithm, where only Line T detects a broken conductor 39.5 ms after the fault occurrence. The algorithms for Lines L and R correctly do not detect a broken conductor fault.

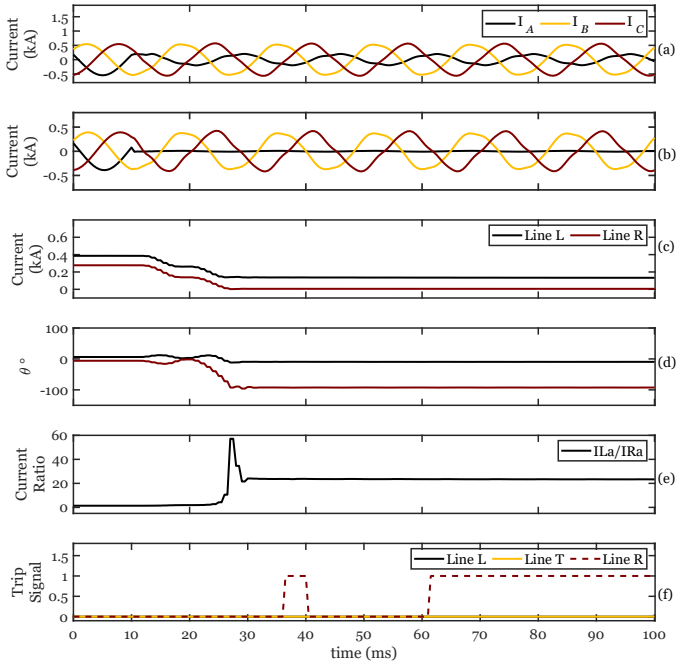

Fig. 5. Simulation results for broken conductor at Line R: (a) Line L instantaneous current, (b) Line R instantaneous current, (c) Lines L and R phase a RMS current, (d) impedance angle for phase a, (e) $\frac{I_{La}}{I_{Ra}}$, and (f) the trip signals.

C. Broken Conductor at Line R

Fig. 5 shows results for a broken conductor fault at Line R occurring at $t = 10$ ms. Fig. 5(a) shows the three-phase current of Line L, where the phase a peak current value decreases to 35.48% of the pre-fault value; however, the other two phases do not change significantly. Fig. 5(b) shows the three-phase

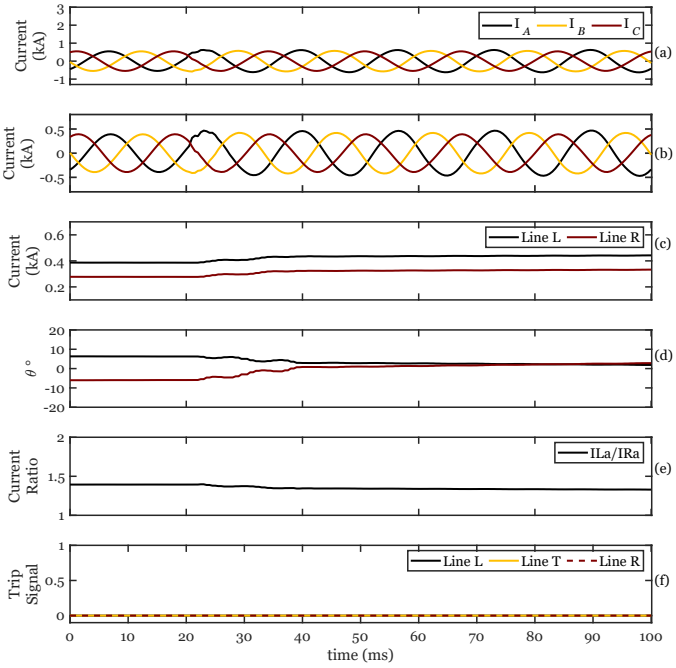

Fig. 6. Simulation results for broken conductor at Line 57: (a) Line L instantaneous current, (b) Line R instantaneous current, (c) Lines L and R phase a RMS current, (d) impedance angle for phase a, (e) $\frac{I_L a}{I_R a}$, and (f) the trip signals.

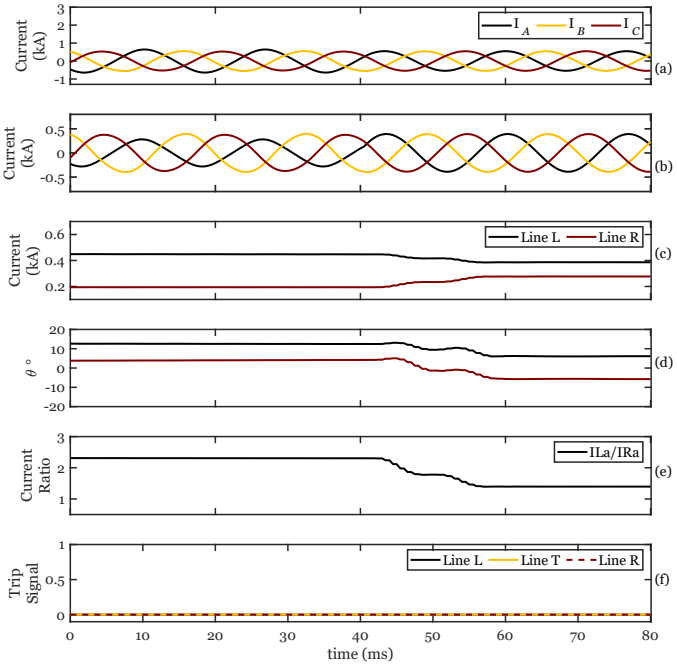

Fig. 7. Simulation results for single-phase load rejection: (a) Line L instantaneous current, (b) Line R instantaneous current, (c) Lines L and R phase a RMS current, (d) impedance angle for phase a, (e) $\frac{I_L a}{I_R a}$, and (f) the trip signals.

current of Line R, where the phase a current decreases significantly since only the capacitive charging current goes through phase a; however, the other two phases' peak current values do not change significantly. Fig. 5(c) shows the RMS values of the phase a currents of buses 7 and 8, where I_{La} decreases from 0.386 kA to 0.133 kA and I_{Ra} decreases from 0.277 kA to 0.0057 kA. Fig. 5(d) shows the phase a impedance angle seen from buses 7 and 8, where θ_{Bus7a} decreases from 6.36° to −9.45° and θ_{Bus8a} decreases from −6.11° to −92.49°. Fig. 5(e) shows the ratio of the phase a current magnitude of bus 7 to bus 8, where it increases from 1.39 to 23.36 in the steady state. Fig. 5(f) shows the trip signal for each algorithm, where only Line R detects a broken conductor with certainty 51.5 ms after the fault occurrence. The Line L and T algorithms correctly do not detect a broken conductor fault.

D. Broken Conductor at Adjacent Line

Fig. 6 shows results for a broken conductor fault at phase a of Line 57, adjacent line, occurring at $t = 20$ ms. Fig. 6(a) and (b) show the three-phase current for Lines L and R, where only the phase a current gets distorted after the broken conductor at Line 57, connecting buses 5 and 7. Fig. 6(c) shows that the RMS values of the phase a currents of Lines L and R, where they increase from 0.335 A to 0.43 kA and 0.27 kA to 0.32 kA, respectively. Fig. 6(d) shows the phase a impedance angle seen from buses 7 and 8, where it decreases from 6.2° to 2.8° and increases from −5.9° to 1°, respectively. Fig. 6(e) shows $\frac{I_{La}}{I_{Ra}}$, which does not change after the fault occurrence. Fig. 6(f) shows the trip signal for Lines L, T, and R, where the algorithm does not detect the fault at the adjacent zone.

E. Single-Phase Load Rejection

Fig. 7 shows results for a single-phase load rejection at $t = 40$ ms connected to Bus 10 at phase a, 30 MW and 10 MVAr. Fig. 7(a) and (b) show the three-phase current for Lines L and R, where only the phase a current changes after the load disconnection at $t = 40$ ms. Fig. 7(c) shows that the RMS values of the phase a currents of Lines L and R, where they decreases from 0.44 A to 0.38 kA and increases from 0.19 kA to 0.27 kA, respectively. Fig. 7(d) shows the phase a impedance angle seen from buses 7 and 8, where it decreases from 12.5° to 6.01° and increases from 4.08° to −5.72°, respectively. Fig. 7(e) shows $\frac{I_{La}}{I_{Ra}}$, which decreases 2.3 to 1.39. Fig. 7(f) shows the trip signal for Lines L, T, and R, where the algorithm does not consider a large single-phase load rejection as a broken conductor fault, demonstrating the algorithm's security.

F. Single Phase to Ground Short-Circuit Fault

Fig. 8 shows the results of a phase a to ground fault at the tapped bus shown in Fig. 1, starting at $t = 20$ ms. The fault resistance is 200 Ω and the fault duration is 200 ms. Fig. 8(a) and (b) show the three-phase current at Lines L and R respectively. Fig. 8(c) shows the RMS values of the phase a current of Lines L and R, where I_{La} increases from 0.386 kA to 0.577 kA and I_{Ra} decreases from 0.277 kA to 0.044 kA and Fig. 8(d) shows the phase a impedance angle seen from buses 7 and 8, where θ_{Bus7a} increases from 6.26° to 9.45° and θ_{Bus8a} increases from −5.92° to 9.45°. Fig. 8(e) shows the $\frac{I_{La}}{I_{Ra}}$, where it increases after fault occurrence and returns to its pre-fault value after the fault clearance. Fig. 8(f) shows

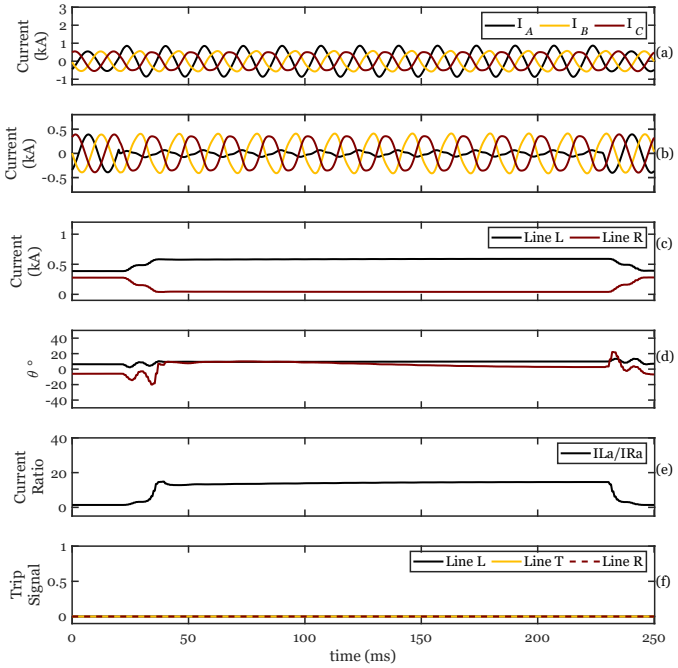

Fig. 8. Simulation results for a phase a to ground short-circuit faults: (a) Line L instantaneous current, (b) Line R instantaneous current, (c) Lines L and R phase a RMS current, (d) impedance angle for phase a, (e) $\frac{I_{La}}{I_{Ra}}$, and (f) the trip signals.

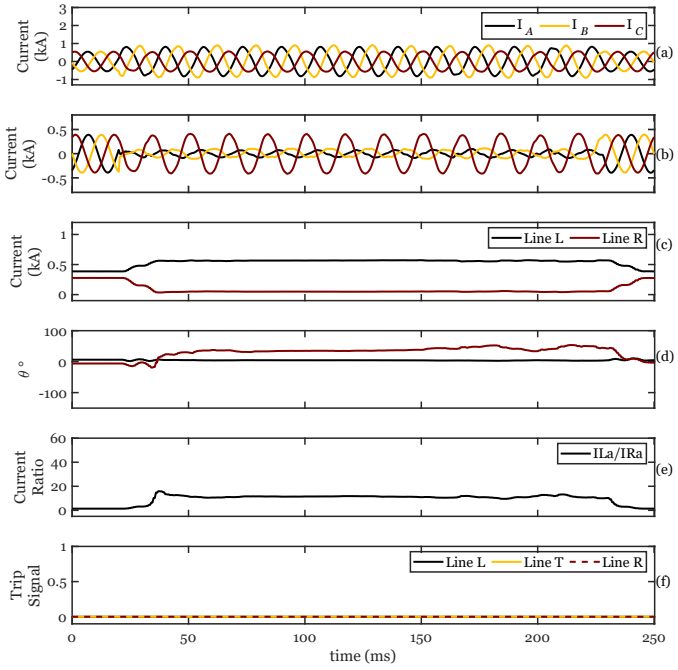

Fig. 9. Simulation results for a phases a and b to ground short-circuit fault: (a) Line L instantaneous current, (b) Line R instantaneous current, (c) Lines L and R phase a RMS current, (d) impedance angle for phase a, (e) $\frac{I_{La}}{I_{Ra}}$, and (f) the trip signals.

the trip signal for each algorithm, where all the algorithms correctly do not send a trip signal.

G. Two-Phase to Ground Short-Circuit Fault

Fig. 9 shows results of a phase a and b to ground fault at the tapped bus shown in Fig. 1(b), starting at $t = 20$ ms. The

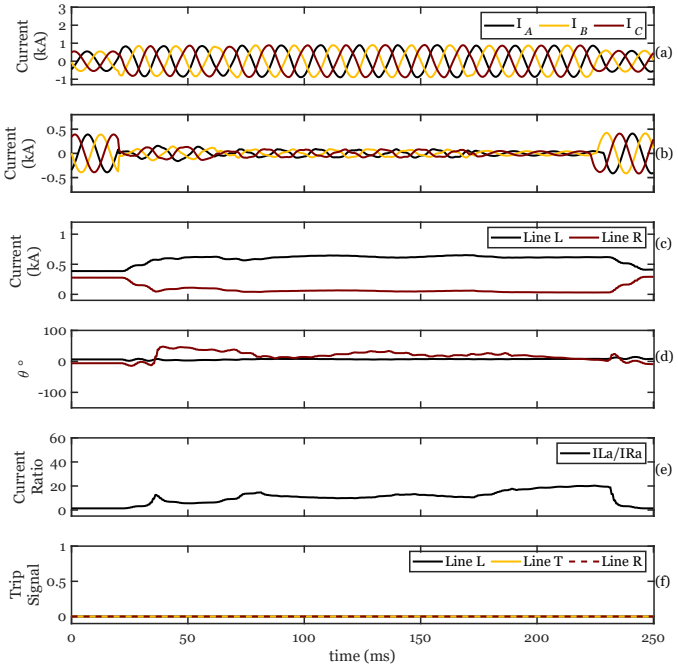

Fig. 10. Simulation results for a three-phase to ground short-circuit fault: (a) Line L instantaneous current, (b) Line R instantaneous current, (c) Lines L and R phase a RMS current, (d) impedance angle for phase a, (e) $\frac{I_{La}}{I_{Ra}}$, and (f) the trip signals.

fault resistance is 200 Ω and the fault is cleared at $t = 220$ ms. Fig. 9(a) and (b) show the three-phase current at Lines L and R, respectively. The phase b and c current magnitudes at Line L increase and the phase b and c current magnitudes at Line R decrease. Fig. 9(c) shows the RMS values of the phase a current of Lines L and R, where I_{La} increases from 0.386 kA to 0.596 kA and I_{Ra} decreases from 0.277 kA to 0.048 kA and Fig. 9(d) shows the phase a impedance angle seen from buses 7 and 8, where θ_{Bus7a} decreases from 6.26° to 4.46° and θ_{Bus8a} increases from −5.92° to 35.13°. Fig. 9(e) shows the ratio of the phase a current magnitude of Line L to that of Line R. Fig. 9(f) shows the trip signal for each algorithm, where all the algorithms correctly do not send a trip signal.

H. Three-Phase to Ground Short-Circuit Fault

Fig. 10 shows results of a three-phase to ground fault through a 200 Ω resistance at the tapped bus shown in Fig. 1(b), starting at $t = 20$ ms and clearing at $t = 220$ ms. Fig. 10(a) and (b) show the three-phase current at Lines L and R, respectively. Line L three-phase current magnitude increases and the Line R three-phase current magnitude decreases. Fig. 10(c) shows the RMS values of the phase a current of Lines L and R, where I_{La} increases from 0.388 kA to 0.64 kA and I_{Ra} decreases from 0.277 kA to 0.064 kA and Fig. 10(d) shows the phase a impedance angle seen from buses 7 and 8, where θ_{Bus7a} decreases from 6.26° to 4.53° and θ_{Bus8a} increases from −5.92° to 42.48° followed by a decrease to 7.76°. Fig. 10(e) shows the ratio of the phase a current magnitude of Line L to that of Line R. Fig. 10(f) shows the trip

signal for each algorithm, where all the algorithms correctly do not send a trip signal.

V. Conclusion

The presence of tapped lines in a transmission system and the integration of IBRs makes broken conductor detection challenging. An undetected broken conductor fault can lead to a wildfire, increasing the importance of developing fast and reliable broken conductor detection and fault location. This work proposes using communication to implement a fast fault detection and location algorithm for broken conductors in tapped transmission lines. The proposed method's dependability and security are tested under various cases, such as broken conductor at tap lines, broken conductor at adjacent lines, single-phase and three-phase short circuit faults, and a sudden single-phase load disconnection at the tapped line using the modified IEEE 9-bus system with two-grid-following IBRs. Accurate fault location helps disconnect only the minimal affected area and increase the reliability of the grid. The algorithm detects the fault and locates it in less than 55 ms. Future work includes developing algorithms for high-impedance fault detection as well.

References

[1] Y. Gong, G. Juvekar, and K. Dase, "Zero-setting broken conductor detection method using local measurements only," in *Annual Western Protective Relay Conference*, Spokane, WA, Oct. 2023.

[2] M. Beikbabaei, M. Lindemann, M. Heidari Kapourchali, and A. Mehrizi-Sani, "Machine learning–based protection and fault identification of 100% inverter-based microgrids," in *International Symposium on Industrial Electronics (ISIE)*, Ulsan, South Korea, Jun. 2024.

[3] P. Gadde and S. M. Brahma, "Topology-agnostic, scalable, self-healing, and cost-aware protection of microgrids," *IEEE Transactions on Power Delivery*, vol. 37, no. 4, pp. 3391–3400, Nov. 2021.

[4] D. V. João, H. G. B. Souza, and M. A. I. Martins, "Broken conductor fault detection using symmetrical components in distribution power systems - an implementation case," in *IEEE Innovative Smart Grid Technologies Conference - Latin America (ISGT Latin America)*, Lima, Peru, Oct. 2021.

[5] B. Alexander, A. Mehrizi-Sani, and A. Mohammadhassani, "Protection of inverter-based resources under open-circuit breaker malfunction," in *IEEE Innovative Smart Grid Technologies Conference (ISGT)*, Washington, DC, Feb. 2024.

[6] A. Mohammadhassani and A. Mehrizi-Sani, "Open-circuit submodule fault diagnosis in MMCs using support vector machines," *IET Generation, Transmission & Distribution*, vol. 16, no. 24, pp. 5015–5025, Dec. 2022.

[7] O. Gashteroodkhani, M. Majidi, and M. Etezadi-Amoli, "Fire hazard mitigation in distribution systems through high impedance fault detection," *Electric Power Systems Research*, vol. 192, p. 106928, Mar. 2021.

[8] N. Rhodes, L. Ntaimo, and L. Roald, "Balancing wildfire risk and power outages through optimized power shut-offs," *IEEE Transactions on Power Systems*, vol. 36, no. 4, pp. 3118–3128, Dec. 2020.

[9] A. Ghaderi, H. L. Ginn, and H. A. Mohammadpour, "High impedance fault detection: A review," *Electric Power Systems Research*, vol. 143, pp. 376–388, Feb. 2017.

[10] A. Sultan, G. Swift, and D. Fedirchuk, "Detecting arcing downed-wires using fault current flicker and half-cycle asymmetry," *IEEE Transactions on Power Delivery*, vol. 9, no. 1, pp. 461–470, Aug. 1994.

[11] C. Kim, B. Russell, and K. Watson, "A parameter-based process for selecting high impedance fault detection techniques using decision making under incomplete knowledge," *IEEE Transactions on Power Delivery*, vol. 5, no. 3, pp. 1314–1320, Aug. 1990.

[12] U.S. department of agriculture, "Forest service report rising firefighting costs raises alarms[online]," Sep. 2021. [Online]. Available: https://www.usda.gov/media/press-releases/2015/08/05/forest-service-report-rising-firefighting-costs-raises-alarms

[13] A. Jalilian, K. M. Muttaqi, and D. Sutanto, "A novel voltage clamping-based overvoltage protection strategy to avoid spurious trip of inverter-based resources and eliminate the risk of wildfire following the REFCL operation in compensated networks," *IEEE Transactions on Industry Applications*, vol. 57, no. 5, pp. 4558–4568, Jun. 2021.

[14] A. J. Ali, L. Zhao, and M. H. Kapourchali, "Data-driven-based analysis and modeling for the impact of wildfire smoke on PV systems," *IEEE Transactions on Industry Applications*, vol. 60, no. 2, pp. 2076–2084, Jul. 2023.

[15] K. Dase, S. Harmukh, and A. Chatterjee, "Detecting and locating broken conductor faults on high-voltage lines to prevent autoreclosing onto permanent faults," in *Annual Georgia Tech Protective Relaying Conference*, Atlanta, GA, May 2023.

[16] F. Yang, H. Li, W. Hu, Y. Lei, H. Chen, and Y. Xue, "Identification of single-phase line break fault direction based on local voltage information in small current grounding system considering the impact of DG," *IEEE Access*, vol. 11, pp. 120 754–120 765, Oct. 2023.

[17] L. Zichang, L. Yadong, Y. Yingjie, W. Peng, and J. Xiuchen, "An identification method for asymmetric faults with line breaks based on low-voltage side data in distribution networks," *IEEE Transactions on Power Delivery*, vol. 36, no. 6, pp. 3629–3639, Dec. 2021.

[18] S. H. Al-Ghannam, Y. Khan, U. Ahmad, N. H. Malik, A. A. Al-Arainy, and B. S. Al-Shahrani, "Development of open (broken) conductor detection system for high resistivity areas," in *Saudi Arabia Smart Grid (SASG) conference*, Jeddah, Saudi Arabia, Dec. 2017.

[19] D. Mu, S. Lin, and X. Li, "Traveling wave characteristics based pilot protection scheme for hybrid cascaded HVDC transmission line," *Journal of Modern Power Systems and Clean Energy*, vol. 12, no. 3, pp. 971–980, Jul. 2024.

[20] A. M. Saber, A. Youssef, D. Svetinovic, H. H. Zeineldin, and E. F. El-Saadany, "Cyber-immune line current differential relays," *IEEE Transactions on Industrial Informatics*, vol. 20, no. 3, pp. 3597–3608, Mar. 2024.

[21] A. Ameli, A. Hooshyar, and E. F. El-Saadany, "Development of a cyber-resilient line current differential relay," *IEEE Transactions on Industrial Informatics*, vol. 15, no. 1, pp. 305–318, Apr. 2018.

[22] H. Miller, J. Burger, N. Fischer, and B. Kasztenny, "Modern line current differential protection solutions," in *Annual Conference for Protective Relay Engineers*, College Station, TX, May 2010.

[23] X. Zheng, C. Chao, Y. Weng, H. Ye, Z. Liu, P. Gao, and N. Tai, "High-frequency fault analysis-based pilot protection scheme for a distribution network with high photovoltaic penetration," *IEEE Transactions on Smart Grid*, vol. 14, no. 1, pp. 302–314, Sep. 2022.

[24] Dominion Energy, "Fiber projects [online]," Jul. 2024. [Online]. Available: https://www.dominionenergy.com/projects-and-facilities/electric-projects/energy-grid-transformation/gt-plan-fiber-projects

[25] Illinois Center for a Smarter Grid, "WSCC 9 bus system[online]," Jul. 2024. [Online]. Available: https://icseg.iti.illinois.edu/wscc-9-bus-system/